PERGAMON

International Journal of Solids and Structures 38 (2001) 897–913

INTERNATIONAL JOURNAL OF SOLIDS and STRUCTURES

www.elsevier.com/locate/ijsolstr

Three-dimensional embedded discontinuity model for brittle fracture

G.N. Wells [a,*], L.J. Sluys [b]

[a] *Faculty of Aerospace Engineering, Koiter Institute Delft, Delft University of Technology, P.O. Box 5048, 2600 GA Delft, Netherlands*
[b] *Faculty of Civil Engineering and Geosciences, Koiter Institute Delft, Delft University of Technology, P.O. Box 5048, 2600 GA Delft, Netherlands*

Received 17 September 1999

Abstract

Three-dimensional elements with discontinuous shape functions have been developed to model brittle fracture in unstructured meshes. Through the incorporation of discontinuous shape functions, highly localised deformations can be captured in a coarse finite element mesh. By carefully examining the variational formulation, traction continuity is assured in a weak sense across discontinuities and a discrete constitutive (traction–separation) model is applied. Using discrete constitutive models avoids the need for numerical parameters to achieve mesh objective results with respect to energy dissipation. Further, kinematic enhancements allow objective analysis in unstructured meshes. Examples of three-dimensional analysis are shown to illustrate the performance of the model.

Keywords: Strong discontinuity; Embedded crack; Fracture; Enhanced strain

1. Introduction

In the past, the practical modelling of material failure in three dimensions has been limited by the computational tools available. Two-dimensional models have been extensively applied for analysing fracture in concrete, leaving the effect of the third direction uncertain. The obvious issue for two-dimensional modelling is whether it should be carried out under plane strain or plane stress conditions. This question can only be resolved properly through the comparison of plane stress and plane strain simulations with full three-dimensional analyses. Further, tension experiments on concrete have shown that the fracture process is rarely uniform in the third direction, since cracks generally propagate from one corner, rather than uniformly through the entire depth of a specimen (Van Vliet and Van Mier, 1999). This results in different crack patterns on the front- and rearside of a specimen as well as a potentially curved crack plane even in direct tension tests. Such experimental observations raise questions, of what influence does the non-uniform

* Corresponding author. Fax: +31-15-278-6383.
E-mail address: g.wells@citg.tudelft.nl (G.N. Wells).

0020-7683/01/$ - see front matter
PII: S0020-7683(00)00029-9

fracture in the third direction have on the global response and local failure mode, and also the validity of two dimensional models for fracture.

For continuum modelling of brittle failure, the ill-posed nature of the classical continuum when applied to strain softening type problems leads to results that are heavily dependent on the spatial discretisation, both in terms of energy dissipated in failure and failure mode, making the value of its extension in three dimensions questionable. Enhanced continuum models have been shown to overcome the limitations of the classical continuum for softening problems through the inclusion of higher-order gradient (De Borst et al., 1993) or non-local (Pijaudier-Cabot and Bažant, 1987) terms and an internal length scale to the material description. The inclusion of non-local effects leads to a well-posed set of differential equations, producing results which are objective with respect to the spatial discretisation. However, a common feature of higher-order models is the need for a fine mesh in the failure zone in order to capture the very high strain gradients. A mesh with several elements across the failure zone (depending on the order of the interpolations) is required in order to accurately capture the failure zone. This requires some prior knowledge of where failure will occur and limits the potential of such methods for three-dimensional applications. For practical application of these models, special re-meshing techniques are required to refine the mesh locally in the failure zones (Askes and Sluys, 2000).

The embedment of discontinuities within elements has been proposed as a method of overcoming the mesh dependency of classical continuum models and the dependency of discrete models on mesh alignment. Effectively, localised failure is treated as a discrete phenomenon, but contained within a continuum framework. The embedment of the discontinuity within elements allows a crack to propagate arbitrarily through a mesh, unlike conventional discrete models where possible crack paths are restricted to inter-element boundaries. The damaging process of a material is viewed here from a level where it can be compressed onto a line. Unlike enhanced continuum models, the embedment of discontinuities is ideal for situations where the typical finite element size is several times larger than the identifiable length scale of the material. By carefully examining the variational formulation, the discontinuities can then be incorporated within standard finite elements.

By formulating the embedded discontinuity as a special case of continuum constitutive laws (subject to several conditions), considerable insight can be gained into the development of discontinuities. Simo et al. (1993) linked the development of strong discontinuities with the loss of ellipticity of governing differential equations of the classical continuum model. This allows the application of not only cohesive crack type models, as have been used in the past for discrete crack modelling, but also provides a general framework for other types of localised failure (Armero and Garikipati, 1996).

The discontinuity formulated here in three dimensions contains a jump in the displacement field (so-called *strong* discontinuity) (Oliver and Simo, 1994; Lotfi and Shing, 1995; Armero and Garikipati, 1996; Larsson and Runesson, 1996). The alternative is a *weak* discontinuity where a jump is added in the strain field (Ortiz et al., 1987, Belytschko et al., 1988; Sluys and Berends, 1998). The *weak* approach allows the direct application of continuum constitutive laws, since Dirac-delta distributions do not appear in the strain field. This method is applicable in problems that involve an obvious jump in strain rates (such as shear bands in metals and soils), but it requires a length scale parameter to define the width of the strain jump and as yet has been unable to overcome mesh alignment dependency (Sluys, 1997). Through the addition of specially constructed enhanced shape functions in the strong discontinuity model, elements are more able to properly represent the highly localised modes that prelude failure.

The extension of embedded discontinuities to three dimensions is a natural progression to exploit the advantages of the embedded model. However, three-dimensional implementation places extra demands on the robustness and is computationally challenging. The increased number of alternative equilibrium paths as a crack propagates in three dimensions (particularly through unstructured meshes) makes the solution procedure critical. In order to construct embedded discontinuities within finite elements, here elements are kinematically enhanced to allow proper reproduction of the localised deformation modes. Then, the three-

field variational statements are extended to include a displacement jump. The resulting Dirac-delta distributions are explicitly integrated along the discontinuity, providing admissible variations of the enhanced modes (test functions) to satisfy traction continuity across the embedded interfaces. Through the explicit integration of the Dirac-delta distributions, no special artificial numerical parameters are required for the numerical implementation. A comparison is made between the approach where enhanced modes are constructed by the examination of the variational statements only (symmetric approach) and the approach which includes kinematically constructed enhancements (non-symmetric). The finite element analysis here is carried out using the four-noded tetrahedron as the underlying element. The ability of this model to produce mesh-objective results in three-dimensional problems as well as its ability to model curved cracking is examined.

2. Kinematic description

Consider a body Ω crossed by a material discontinuity (Fig. 1). The body can be decomposed into two sub-domains, Ω^+ and Ω^-, which lie on either side of a discontinuity Γ_d. A vector normal to the discontinuity Γ_d is defined as $\mathbf{n}_d$. In addition, it is useful to define a sub-domain of Ω, Ω^d, which is centred on the discontinuity.

2.1. Discontinuous displacement field

In order to describe the displacement field of a body crossed by a discontinuity, the displacement field can be decomposed into continuous and discontinuous parts,

$$\mathbf{u}(\mathbf{x},t) = \hat{\mathbf{u}}(\mathbf{x},t) + \mathscr{H}_{\Gamma_d}[\![\mathbf{u}(\mathbf{x},t)]\!], \tag{1}$$

where $\hat{\mathbf{u}}(\mathbf{x},t)$ is the regular, continuous part of the displacement field, $\mathscr{H}_{\Gamma_d}$ is the Heaviside function centred on the discontinuity ($\mathscr{H}_{\Gamma_d} = 1$ if $\mathbf{x} \in \Omega^+$, $\mathscr{H}_{\Gamma_d} = 0$ if $\mathbf{x} \in \Omega^-$) and $[\![\mathbf{u}(\mathbf{x},t)]\!]$ is a continuous function on Ω. The vector $[\![\mathbf{u}(\mathbf{x},t)]\!]$ at the discontinuity ($\mathbf{x} \in \Gamma_d$) gives the components of the displacement jump across the discontinuity.

The displacement decomposition carried out above uses two continuous functions ($\hat{\mathbf{u}}$ and $[\![\mathbf{u}]\!]$) which are both potentially non-zero on the boundary. In the context of finite element analysis, this means that when imposing boundary conditions both $\hat{\mathbf{u}}$ and $[\![\mathbf{u}]\!]$ must be taken into account. A more suitable decomposition is one which requires that the enhanced component of the displacement field be zero on the boundary. Therefore, only the regular part of the then displacement field need be taken into account at the boundaries (Oliver and Simo, 1994).

$$\mathbf{u}(\mathbf{x},t) = \hat{\mathbf{u}}(\mathbf{x},t) + (\mathscr{H}_{\Gamma_d} - \varphi(\mathbf{x}))[\![\mathbf{u}(\mathbf{x},t)]\!]. \tag{2}$$

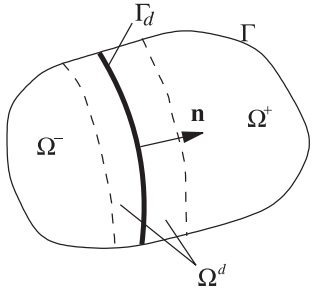

Fig. 1. Body crossed by a material discontinuity.

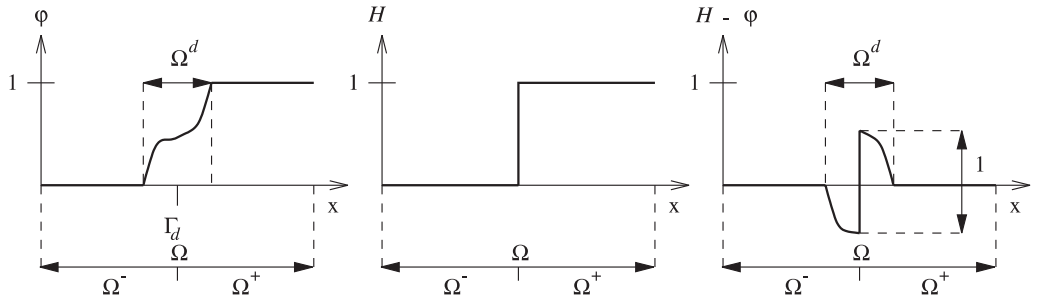

Fig. 2. One-dimensional displacement decomposition.

In Eq. (2), $\varphi(\mathbf{x})$ is a continuous function obeying

$$\varphi(\mathbf{x}) = \begin{cases} 1, & \mathbf{x} \in \ \Omega^+ \setminus \Omega^{\mathrm{d}}, \\ 0, & \mathbf{x} \in \ \Omega^- \setminus \Omega^{\mathrm{d}}. \end{cases} \tag{3}$$

Taking the gradient of Eq. (2) yields the strain field. In the context of brittle fracture, infinitesimal strains are assumed throughout. All gradients ∇ are taken to be the symmetric part only.

$$\boldsymbol{\varepsilon}(\mathbf{x},t) = \underbrace{\nabla\hat{\mathbf{u}}(\mathbf{x},t)}_{\text{regular part}} + \underbrace{((\delta_{\Gamma_{\mathrm{d}}}\mathbf{n}_{\mathrm{d}}(\mathbf{x}) - \nabla\varphi(\mathbf{x})) \otimes [\![\mathbf{u}(\mathbf{x},t)]\!]) + (\mathscr{H}_{\Gamma_{\mathrm{d}}} - \varphi(\mathbf{x}))(\nabla[\![\mathbf{u}(\mathbf{x},t)]\!])}_{\text{enhanced part}}. \tag{4}$$

The one-dimensional displacement decomposition for Eq. (2) is shown in Fig. 2.

3. Finite element implementation

In keeping with finite element convention, discretised forms of the initial value problem are expressed in matrix–vector form where the strain and stress tensors are represented as column vectors ($\boldsymbol{\varepsilon} = (\varepsilon_{11}, \varepsilon_{22}, \varepsilon_{33}, 2\varepsilon_{12}, 2\varepsilon_{23}, 2\varepsilon_{31})^{\mathrm{T}}$, $\boldsymbol{\sigma} = (\sigma_{11}, \sigma_{22}, \sigma_{33}, \sigma_{12}, \sigma_{23}, \sigma_{31})^{\mathrm{T}}$). For fields which are not discretised, tensor notation is used. The discretised kinematic fields for a body containing a discontinuity can be written as follows:

$$\mathbf{u}(\mathbf{x}) = \mathbf{N}_a(\mathbf{x})\mathbf{a} + \mathbf{N}_\alpha(\mathbf{x})\boldsymbol{\alpha}, \tag{5a}$$

$$\boldsymbol{\varepsilon}(\mathbf{x}) = \mathbf{B}(\mathbf{x})\mathbf{a} + \mathbf{G}(\mathbf{x})\boldsymbol{\alpha}, \tag{5b}$$

where $\mathbf{N}_a$ and $\mathbf{B}$ are the normal displacement and strain interpolation matrices, respectively, $\mathbf{N}_\alpha$ and $\mathbf{G}$ are the displacement and strain interpolation matrices, respectively, for the enhanced modes, $\mathbf{a}$ is the nodal displacement and $\boldsymbol{\alpha}$ is the displacement associated with enhanced degrees of freedom at the discontinuity. Further, it is necessary to define a matrix which contains the normal components to the discontinuity.

$$\mathbf{n}^{\mathrm{T}} = \begin{bmatrix} n_x & 0 & 0 & n_y & 0 & n_z \\ 0 & n_y & 0 & n_x & n_z & 0 \\ 0 & 0 & n_z & 0 & n_y & n_x \end{bmatrix}. \tag{6}$$

3.1. Mixed variational formulation

To construct a finite element that incorporates a displacement discontinuity, it is necessary to examine the three-field variational statements. This is done starting from a modified form of the three-field variational statements that include the so-called *enhanced strains* (Simo and Rifai, 1990) where the strain field $\boldsymbol{\varepsilon}$ is decomposed into compatible $\nabla\mathbf{u}$ and incompatible $\tilde{\boldsymbol{\varepsilon}}$ parts. By considering the appearance of Dirac-delta

distributions in the *enhanced* strain field and properties of the Dirac-delta distribution ($\int_{\Omega_e} \phi \delta_{\Gamma_d} \mathrm{d}\Omega = \int_{\Gamma_e} \phi \, \mathrm{d}\Gamma$), the variational statements can be extended to include a displacement jump (Larsson and Runesson, 1996; Wells and Sluys, 2000),

$$\int_\Omega \nabla \boldsymbol{\eta} : \frac{\partial W(\mathbf{x}, \nabla \mathbf{u} + \tilde{\boldsymbol{\varepsilon}}^{\mathbf{k}})}{\partial \boldsymbol{\varepsilon}} \, \mathrm{d}\Omega - W^{\mathrm{ext}}(\boldsymbol{\eta}) = 0, \tag{7a}$$

$$\int_\Omega \boldsymbol{\tau} : \tilde{\boldsymbol{\varepsilon}}_c \, \mathrm{d}\Omega + \int_{\Gamma_d} (\boldsymbol{\tau} \boldsymbol{v}_d) \cdot \mathbf{n}_d \, \mathrm{d}\Gamma = 0, \tag{7b}$$

$$\int_\Omega \tilde{\boldsymbol{\gamma}}_c : \left(-\boldsymbol{\sigma} + \frac{\partial W(\mathbf{x}, \nabla \mathbf{u} + \tilde{\boldsymbol{\varepsilon}}^{\mathbf{k}})}{\partial \boldsymbol{\varepsilon}} \right) \mathrm{d}\Omega + \int_{\Gamma_d} \left[\left(-\boldsymbol{\sigma} + \frac{\partial W(\mathbf{x}, \nabla \mathbf{u} + \tilde{\boldsymbol{\varepsilon}}^{\mathbf{k}})}{\partial \boldsymbol{\varepsilon}} \right) \boldsymbol{\eta}_d \right] \cdot \mathbf{n}_d \, \mathrm{d}\Gamma = 0, \tag{7c}$$

where $(\boldsymbol{\eta}, \tilde{\boldsymbol{\gamma}}, \boldsymbol{\tau}) \in (V \times \tilde{E} \times S)$ are all variations of displacements, strains and stresses respectively and $(\mathbf{u}, \tilde{\boldsymbol{\varepsilon}}, \boldsymbol{\sigma}) \in (V \times \tilde{E} \times S)$ are the actual displacements, strains and stresses respectively with $(V \times \tilde{E} \times S)$ the spaces of all displacement, strain and stress fields. The actual displacement jump across a discontinuity is denoted by $\boldsymbol{v}_d$ and variations of the jump are denoted $\boldsymbol{\eta}_d$. The stresses coming from the constitutive law are given by $\partial W(\mathbf{x}, \nabla \mathbf{u} + \tilde{\boldsymbol{\varepsilon}}^k)/\partial \boldsymbol{\varepsilon}$.

3.1.1. Enhanced interpolations

The *enhanced* strain interpolation matrix, corresponding to $\mathbf{G}$ in Eq. (5b), can be formed for a single element crossed by a discontinuity from the enhanced part of the strain field in Eq. (4). By assuming that the displacement jump function $[\![\mathbf{u}(\mathbf{x}, t)]\!]$ is a constant function over an element (Ω_e), part of the right-hand side of the enhanced strain field in Eq. (4) disappears ($\nabla [\![\mathbf{u}(\mathbf{x}, t)]\!]) = \mathbf{0}$, $\mathbf{x} \in \Omega_e$). In finite element terms, this is equivalent to choosing the function ($\mathscr{H}_{\Gamma_d} - \varphi(\mathbf{x})$) as the shape function approximating the displacement jump. Then, for the three-dimensional case,

$$\mathbf{G}_e(\mathbf{x}) = \begin{bmatrix} \delta_{\Gamma_d} n_x - \frac{\partial \varphi(\mathbf{x})}{\partial x} & 0 & 0 \\ 0 & \delta_{\Gamma_d} n_y - \frac{\partial \varphi(\mathbf{x})}{\partial y} & 0 \\ 0 & 0 & \delta_{\Gamma_d} n_z - \frac{\partial \varphi(\mathbf{x})}{\partial z} \\ \delta_{\Gamma_d} n_y - \frac{\partial \varphi(\mathbf{x})}{\partial y} & \delta_{\Gamma_d} n_x - \frac{\partial \varphi(\mathbf{x})}{\partial x} & 0 \\ 0 & \delta_{\Gamma_d} n_z - \frac{\partial \varphi(\mathbf{x})}{\partial z} & \delta_{\Gamma_d} n_y - \frac{\partial \varphi(\mathbf{x})}{\partial y} \\ \delta_{\Gamma_d} n_z - \frac{\partial \varphi(\mathbf{x})}{\partial z} & 0 & \delta_{\Gamma_d} n_x - \frac{\partial \varphi(\mathbf{x})}{\partial x} \end{bmatrix}. \tag{8}$$

The above interpolation has been applied successfully for two dimensional analysis with constant strain triangular elements (Armero and Garikipati, 1996; Oliver, 1996b; Wells and Sluys, 2000); however, it requires some modification for robust three-dimensional implementation with the four-noded tetrahedral element. The conditions for the function $\varphi(\mathbf{x})$ in Eq. (3) must be supplemented by the condition that displacements on each side of the discontinuity are constant along the discontinuity within an element. That is, the enhanced displacements $\boldsymbol{\alpha}$ are constant along the discontinuity within each element. To do this, the regular part of the enhanced shape functions are formed according to the conditions in Eq. (3), then rotated into a local coordinate system aligned with the normal to the discontinuity and the shape function components orthogonal to the discontinuity normal are removed. The shape functions are then rotated back to the global coordinate system. The requirement that the enhanced displacements be constant along the discontinuity within an element is reasonable when considering the constant strain field of the four-noded tetrahedral element. This modification provides almost exactly the same response as with the unmodified $\mathbf{G}_e$ matrix, but leads to a much more robust procedure. In a simple cube patch of elements in tension, failing to remove orthogonal components from the enhanced shape functions results in excessive lateral sliding on the

embedded interfaces and very poor convergence behaviour. This arises particularly in the case when two nodes of a four-noded tetrahedron fall on each side of the discontinuity. Fig. 3 illustrates the cases of linearly varying and constant displacements along a discontinuity. For simplicity, it is illustrated using a triangular element.

Next, in order to ensure traction continuity across discontinuities, the variational statements must be examined. A special formulation is exploited here, first used by Simo et al. (1993), akin to making the space of admissible strains different to the space of admissible strain variations. The resulting system of equations is non-symmetric, but allows traction continuity to be neatly satisfied while utilising the kinematically formed shape functions in Eq. (8).

Following the enhanced assumed strain methodology, the enhanced strain field is assumed to be orthogonal to the stress field, automatically satisfying Eq. (7b). This then allows the stress field to be eliminated from the remaining variational statements. Eq. (7c) can then be rephrased as

$$\int_{\Omega} \tilde{\gamma}_c : \frac{\partial W(\mathbf{x}, \nabla \mathbf{u} + \tilde{\boldsymbol{\varepsilon}}^k)}{\partial \boldsymbol{\varepsilon}} \, \mathrm{d}\Omega + \int_{\Gamma_\mathrm{d}} \left(\frac{\partial W(\mathbf{x}, \nabla \mathbf{u} + \tilde{\boldsymbol{\varepsilon}}^k)}{\partial \boldsymbol{\varepsilon}} \boldsymbol{\eta}_\mathrm{d} \right) \cdot \mathbf{n}_\mathrm{d} \, \mathrm{d}\Gamma = 0. \tag{9}$$

Assuming a straight discontinuity within an element ($\mathbf{n}_\mathrm{d}$ is constant over Ω_e) and a piecewise constant strain field (an exact assumption for constant strain elements), taking into account that to pass the patch test (Taylor et al., 1986), Eq. (9) must hold for an arbitrary constant stress field and the orthogonality requirement must hold for each element, Eq. (9) can be integrated explicitly over an element

$$V_\mathrm{e} \tilde{\gamma}_c + A_\mathrm{e} (\mathbf{n}_\mathrm{d} \otimes \boldsymbol{\eta}_\mathrm{d}) = 0, \tag{10}$$

where V_e is the volume of the element and A_e is the area of the discontinuity plane through the element. Rearranging Eq. (10) gives the expression for the continuous part of the variation of an enhanced strain field on $\Omega_\mathrm{e} \setminus \Gamma_\mathrm{d}$:

$$\tilde{\gamma}_c = -\frac{A_\mathrm{e}}{V_\mathrm{e}} (\mathbf{n}_\mathrm{d} \otimes \boldsymbol{\eta}_\mathrm{d}). \tag{11}$$

Now, the virtual work equation (7a) and Eq. (9) give two weak equilibrium equations for an element containing a discontinuity,

$$\int_{\Omega} \nabla \boldsymbol{\eta} : \frac{\partial W(\mathbf{x}, \nabla \mathbf{u} + \tilde{\boldsymbol{\varepsilon}}^\mathbf{k})}{\partial \boldsymbol{\varepsilon}} \, \mathrm{d}\Omega = W^{\mathrm{ext}}(\boldsymbol{\eta}), \tag{12a}$$

$$\int_{\Omega_\mathrm{e} \setminus \Gamma_\mathrm{d}} \tilde{\gamma}_c : \frac{\partial W(\mathbf{x}, \nabla \mathbf{u} + \tilde{\boldsymbol{\varepsilon}}^\mathbf{k})}{\partial \boldsymbol{\varepsilon}} \, \mathrm{d}\Omega + \int_{\Gamma_\mathrm{d}} \mathbf{t}_{\Gamma_{\mathrm{d,e}}} \cdot \boldsymbol{\eta}_\mathrm{d} \mathrm{d}\Gamma = 0, \tag{12b}$$

where $\mathbf{t}_{\Gamma_{\mathrm{d,e}}}$ comes from a discrete traction–separation law.

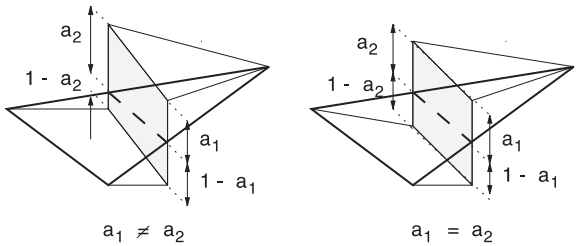

Fig. 3. Triangular element with (a) linearly varying and (b) constant displacements along the discontinuity.

3.2. Linearised equations

In matrix form, the continuous part of the variation of an enhanced strain field in Eq. (11) can be expressed as

$$\mathbf{G}_{\mathrm{e}}^{*} = \left(-\frac{A_{\mathrm{e}}}{V_{\mathrm{e}}} \right) \mathbf{n}. \tag{13}$$

Note that $\mathbf{n}$ is a matrix defined in Eq. (6), rather than the normal vector $\mathbf{n}_{\mathrm{d}}$. Now, for updating stresses, the kinematically constructed interpolation $\mathbf{G}$ in Eq. (8) and the material tangent matrix $\mathbf{D}$ are used:

$$\dot{\boldsymbol{\sigma}} = \mathbf{D}(\mathbf{B}\dot{\mathbf{a}} + \mathbf{G}\dot{\boldsymbol{\alpha}}). \tag{14}$$

Effectively, in Eqs. (12a) and (12b), the enhanced strain field $\tilde{\boldsymbol{\varepsilon}}$ is not necessarily the same as the variation of the enhanced strain $\tilde{\boldsymbol{\gamma}}$. For this reason, in the variational statements, the enhanced strain used in calculating stresses $\tilde{\boldsymbol{\varepsilon}}^{k}$ has been denoted differently to the enhanced strain field that appears explicitly $\tilde{\boldsymbol{\varepsilon}}$. This leads to, in general, a non-symmetric element stiffness matrix irrespective of the material model used. It is possible to use the matrix $\mathbf{G}^{*}$ in the stress update (resulting in a symmetric stiffness matrix (Larsson and Runesson, 1996)), although this provides no kinematic enhancements of the underlying element to assist in overcoming mesh alignment dependency. Although the method adopted here is not variationally consistent (in following the enhanced assumed strain approach to eliminate the stress field from the variational statements, it must be assumed that the spaces of the admissible displacements, strains and stresses are the same as the spaces of the admissible displacement, strain and stress variations), it is able to properly reproduce the localised deformations better. The performances of the symmetric and non-symmetric formulations are compared in Section 5.

Taking variations of the weak equations (12a) and (12b) yield the following discretised non-linear equations:

$$\int_{\Omega_{\mathrm{e}}} \mathbf{B}^{\mathrm{T}} \boldsymbol{\sigma} \, \mathrm{d}\Omega = \mathbf{f}^{\mathrm{ext}}, \tag{15a}$$

$$\int_{\Omega_{\mathrm{e}}} \mathbf{G}^{*\mathrm{T}} \boldsymbol{\sigma} \, \mathrm{d}\Omega + \int_{\Gamma_{\mathrm{d,e}}} \mathbf{t}_{\mathrm{e}} \, \mathrm{d}\Gamma = \mathbf{0}. \tag{15b}$$

Substituting the continuous part of the enhanced strain field Eq. (13) into Eq. (15b) and integrating the tractions over the discontinuity gives

$$A_{\mathrm{e}} \int_{\Omega_{\mathrm{e}}} -\frac{1}{V_{\mathrm{e}}} \mathbf{n}^{\mathrm{T}} \boldsymbol{\sigma} \, \mathrm{d}\Omega + A_{\mathrm{e}} \mathbf{t}_{\mathrm{e}} = 0, \tag{16}$$

which shows that Eq. (15b) imposes traction continuity in a weak sense and that the area of the discontinuity plane acts simply as an integration weight and has *no* influence on the numerical result. Conversely, for the symmetric formulation ($\mathbf{G} = \mathbf{G}^{*}$), since the matrix $\mathbf{G}^{*}$ plays a role in the stress update, the formulation is dependent on the area of the discontinuity plane. In the context of a constant strain element, for the non-symmetric case, the element response is dependent only on the normal to the discontinuity and the position of the discontinuity with respect to the element nodes, whereas with the symmetric formulation, the element response is dependent on the normal to the discontinuity and the area of the discontinuity plane.

Linearising Eqs. (15a) and (15b), gives the stiffness matrix of an element:

$$\begin{bmatrix} \mathbf{K}_{\mathrm{bb,e}} & \mathbf{K}_{\mathrm{bg,e}} \\ \mathbf{K}_{\mathrm{g^{*}b,e}} & \mathbf{K}_{\mathrm{g^{*}g,e}} + \mathbf{K}_{\mathrm{t,e}} \end{bmatrix} \begin{Bmatrix} d\mathbf{a}_{\mathrm{e}} \\ d\boldsymbol{\alpha}_{\mathrm{e}} \end{Bmatrix} = \begin{Bmatrix} \mathbf{f}_{\mathrm{u,e}}^{\mathrm{ext}} \\ \mathbf{0} \end{Bmatrix} - \begin{Bmatrix} \mathbf{f}_{\mathrm{u,e}}^{\mathrm{int}} \\ \mathbf{f}_{\alpha,\mathrm{e}}^{\mathrm{int}} \end{Bmatrix}, \tag{17}$$

where

$$\begin{aligned}
\mathbf{K}_{\mathrm{bb,e}} &= \int_{\Omega_\mathrm{e}} \mathbf{B}_\mathrm{e}^\mathrm{T}\mathbf{D}\mathbf{B}_\mathrm{e}\,\mathrm{d}\Omega,\\
\mathbf{K}_{\mathrm{bg,e}} &= \int_{\Omega_\mathrm{e}} \mathbf{B}_\mathrm{e}^\mathrm{T}\mathbf{D}\mathbf{G}_\mathrm{e}\,\mathrm{d}\Omega,\\
\mathbf{K}_{\mathrm{g^*b,e}} &= \int_{\Omega_\mathrm{e}} \mathbf{G}_\mathrm{e}^{*\mathrm{T}}\mathbf{D}\mathbf{B}_\mathrm{e}\,\mathrm{d}\Omega,\\
\mathbf{K}_{\mathrm{g^*g,e}} &= \int_{\Omega_\mathrm{e}} \mathbf{G}_\mathrm{e}^{*\mathrm{T}}\mathbf{D}\mathbf{G}_\mathrm{e}\,\mathrm{d}\Omega,\\
\mathbf{K}_{\mathrm{t,e}} &= \int_{\Gamma_\mathrm{e}} \mathbf{T}_\mathrm{e}\,\mathrm{d}\Gamma,
\end{aligned} \tag{18}$$

and $\mathbf{T}_\mathrm{e}$ is the matrix that relates displacements and tractions at the discontinuity, ($\dot{\mathbf{t}}_\mathrm{e} = \mathbf{T}_\mathrm{e}\dot{\boldsymbol{\alpha}}_\mathrm{e}$). Note that $\mathbf{G}_\mathrm{e}$ contains only the regular parts of Eq. (8). The enhanced modes ($\boldsymbol{\alpha}_\mathrm{e}$) can be solved at element level by static condensation.

4. Discrete constitutive model

The application of discrete traction–displacement constitutive models allows the phenomenological behaviour of materials to be addressed in a very simple and direct manner. The individual displacement components at the interface provide much information as to the actual current state at the interface (crack opening, sliding, closing, closed). It is possible to address to traction–displacement relationship for each component separately, or to define some type of inter-dependence.

For application here in three dimensions, a relatively simple damage model has been applied. A very intuitive approach is taken by making mode-I and mode-II stiffnesses functions of the normal separation. The traction–separation relationships are constructed entirely in the local n, s, t, coordinate system where n is the normal to the discontinuity and s and t are orthogonal and lie in the plane of the discontinuity (Fig. 4). To form the element stiffness matrix and internal force vector, the tractions $\mathbf{t}$ and traction tangent $\mathbf{T}$ at the discontinuity are rotated back to the global coordinate system.

Since the intended application is for brittle fracture, the normal to the discontinuity is aligned with the major tensile principal stress. When, at the end of a loading step, the major tensile principal stress at an

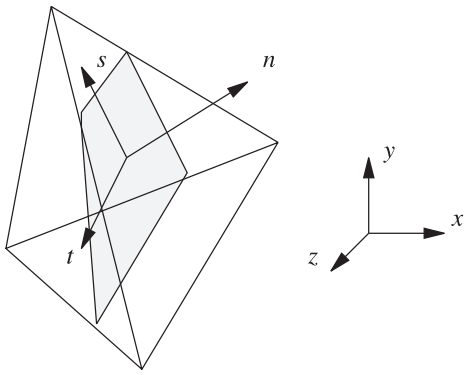

Fig. 4. Local n, s, t coordinate system within a tetrahedral element.

integration point has exceeded the tensile strength of the material, a discontinuity is introduced. Discontinuities are introduced only at the *end* of a loading step since it is undesirable to introduce a discontinuity to a non-equilibrium state. Also, by introducing discontinuities only at the end of a loading increment, the convergence rate of the full Newton–Raphson scheme is quadratic.

4.1. Loading/unloading

The internal variable κ is taken as the maximum normal displacement attained. The loading function is then defined as:

$$f(\alpha_n, \kappa) = \alpha_n - \kappa, \tag{19}$$

where $f \geqslant 0$ indicates loading (growing damage) and $f < 0$ indicates unloading (crack closing). A closed crack is indicated by $\alpha_n < 0$.

For modelling brittle materials such as concrete, from experimental experience, an exponential softening curve is adopted for the normal traction–separation relationship at the interface. The relationship is given in terms of the tensile strength f_t, the fracture energy G_f of the material and the internal variable:

$$t_n = f_t \exp\left(-\frac{f_t}{G_f}\kappa\right). \tag{20}$$

The shear stiffness is given as an exponential function of the internal variable κ,

$$t_{s,t} = d_{\text{int}} \exp(h_s \kappa)\, \alpha_{s,t}, \tag{21}$$

where d_{int} is the initial shear stiffness of the crack ($\kappa = 0$) and h_s reflects the crack shear stiffness at some intermediate stage of damage. For the crack shear stiffness $d_{\kappa=1.0}$ at $\kappa = 1.0$:

$$h_{s,\kappa=1.0} = -\ln(d_{\kappa=1.0}/d_{\text{int}}). \tag{22}$$

For computational efficiency, Eqs. (20) and (21) can be easily differentiated with respect to time to form a consistent tangent. For loading,

$$\begin{Bmatrix} \dot{t}_n \\ \dot{t}_s \\ \dot{t}_t \end{Bmatrix} = \begin{bmatrix} -\frac{f_t^2}{G_f}\exp(-\frac{f_t}{G_f}\kappa) & 0 & 0 \\ -h_s d_{\text{int}} \exp(h_s\kappa)\alpha_s & d_{\text{int}}\exp(h_s\kappa) & 0 \\ -h_s d_{\text{int}} \exp(h_s\kappa)\alpha_t & 0 & d_{\text{int}}\exp(h_s\kappa) \end{bmatrix} \begin{Bmatrix} \dot{\alpha}_n \\ \dot{\alpha}_s \\ \dot{\alpha}_t \end{Bmatrix}. \tag{23}$$

For unloading, the secant stiffness is given by making all off-diagonal terms zero. The (1,1) term in the tangent stiffness is then replaced by $f_t \exp(-f_t/G_f\kappa)/\kappa$. This differs from normal continuum elasticity based damage models since there is no elastic part to unload. Normally, the secant stiffness is given in terms of the elastic tangent $\mathbf{D}^e$ and a damage variable ω, i.e. $\dot{\boldsymbol{\sigma}}_{\text{unloading}} = (1-\omega)\mathbf{D}^e\dot{\boldsymbol{\varepsilon}}$.

To achieve elastic unloading with the embedded discontinuity model, the diagonal terms of the tangent stiffness can simply be made very large. There are an infinite number of ways to take advantage of the very clear information provided by the individual displacements at the discontinuity. An obvious modification of the above model is to allow shear stiffness recovery with crack unloading. Instead of the shear stiffness being a function of the internal variable κ, it could be made a function of the actual normal separation, $t_{s,t} = d_{\text{int}} \exp(h_s\alpha_n)\, \alpha_{s,t}$.

4.2. Closed crack

For a closed crack, full stiffness recovery for both normal and sliding terms is assumed. Since the displacements at the discontinuity contain no elastic part, the crack stiffness terms are made very large in all directions. A closed crack is detected when the normal component of the displacement at the discontinuity

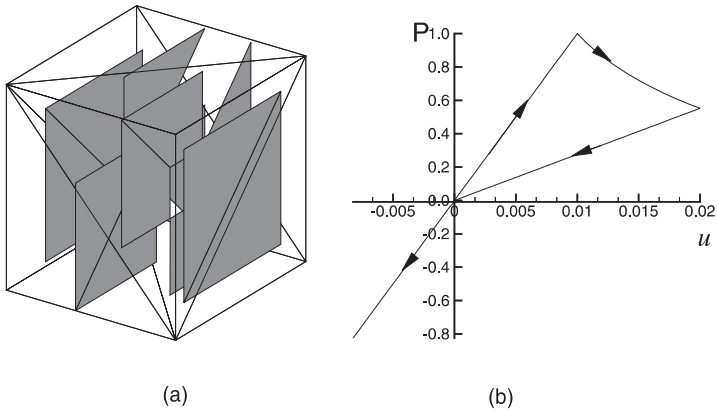

Fig. 5. Unit patch of 12 four-noded tetrahedral elements: (a) embedded discontinuity plane and (b) loading–unloading response.

is less than zero. This physically implies that the two fracture surfaces are pushing against each other. To illustrate the loading–unloading behaviour of the model, a unit patch of 12 four-noded tetrahedral elements is loaded in tension, then unloaded and compressed (Fig. 5).

5. Numerical analysis

In this section, the performance of the embedded model in three dimensions is examined by analysing several different problems. The ability to accurately model failure with coarse meshes allows complex problems to be analysed very efficiently and quickly. Through the linearisation of the constitutive model Eq. (23), quadratic convergence of the full Newton–Raphson solution procedure is observed when loading signs at integration points do not change within a loading increment. This is an enormous advantage when performing large scale calculations.

A difficulty that arises in larger analyses is loading, unloading and reloading at discontinuities within an increment. It has been observed that quadratic convergence behaviour is approached for situations where the loading state at discontinuities changes during the iterative procedure; however, at certain stages in the analysis of larger specimens with fine meshes, one or more discontinuities can begin to oscillate between loading and unloading states, having disastrous consequences for the convergence of the numerical scheme. The robustness of the algorithm can be increased by adopting a modified Newton–Raphson approach when the sign of the loading function is detected to have changed more then once during a loading increment. When this occurs, for the rest of the increment, the secant tangent of the global system is used. Although this increases the robustness of the algorithm by preventing oscillations at the interfaces, the convergence becomes prohibitively slow for large three-dimensional calculations.

5.1. Symmetric versus non-symmetric implementation

To show the difference in response for the symmetric ($\mathbf{G}_e = \mathbf{G}_e^*$) and non-symmetric ($\mathbf{G}_e \neq \mathbf{G}_e^*$) formulations, the load–displacement response and strain energy of a unit patch of elements (Fig. 5) is shown in Fig 6. The fracture energy of the patch was set as 0.02 N mm/mm^2. It can be seen that the symmetric approach grossly overestimates the energy dissipated in the failure process, whereas the non-symmetric model is much closer to the actual fracture energy. In application, the symmetric approach requires some enforcement of crack path continuity, since the position of the discontinuity within the element has a

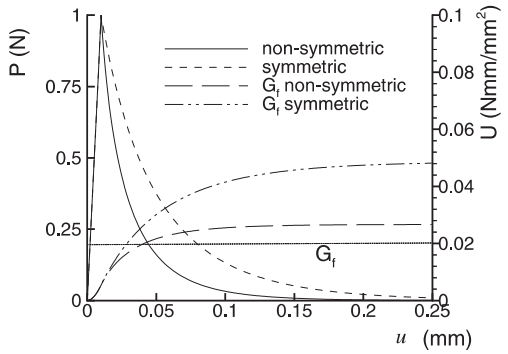

Fig. 6. Load–displacement response and strain energy (U) of a unit patch for symmetric and non-symmetric implementation.

significant effect on the response. Within the simple patch of constant strain elements in Fig 5, the load–displacement response of the symmetric model changes if the location of the integration point within each element is moved. For the non-symmetric model, the result changes only if the domain (Ω^+, Ω^-) to which the element nodes belong to changes. This indicates that the enforcement of crack path continuity is not essential for the non-symmetric model.

5.2. Double notched specimen

To examine the objectivity of the embedded approach, a tension specimen with symmetric notches (Fig. 7) is analysed with two different meshes. The following material properties are adopted: $E = 1.0 \times 10^4$ MPa, $f_t = 1.0$ MPa, $v = 0.1$, $G_f = 0.02$ N mm/mm^2, $d_{int} = 1.0 \times 10^2$ N/mm, $d_{\kappa=1.0} = 1.0 \times 10^{-6}$ N/mm. To avoid

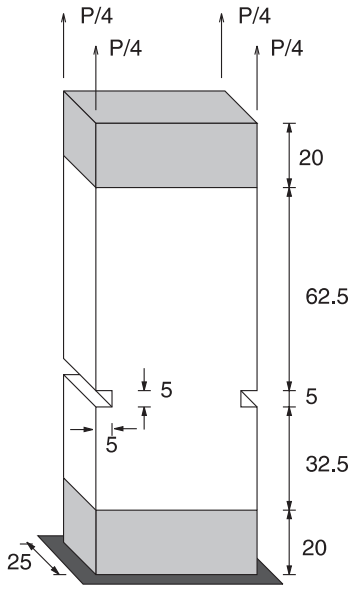

Fig. 7. Double notched specimen (loading plates shaded).

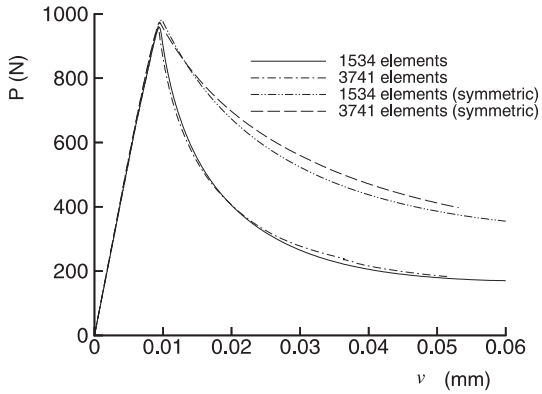

Fig. 8. Load–displacement response of double notched specimen.

any fracture at the supports or loading points, the specimen is placed between two loading plates. The base of the specimen is fully restrained and an equal load is applied at each of the four top corners.

The load–displacement (displacement is taken as the average displacement of the top loading plate) response for two meshes is shown in Fig. 8. It can be seen that the global response of the two meshes (Fig. 9) is nearly identical for the non-symmetric model. Again, the symmetric model shows an overly ductile response. For a third mesh with approximately 6000 elements, it was not possible to calculate a converged solution past the peak load. This can be explained by the cracking pattern shown in Fig. 10 (the visible mesh is only on the boundary of the model). With mesh refinement, the number of parallel layers cracks increases, and it becomes increasingly difficult numerically to find a stable equilibrium branch. Upon refinement of the mesh, near the peak load, the loading function of an increasing number of elements begins to oscillate about zero during the iterative procedure, resulting in a change of sign of the material tangent with each iteration. When this occurs, the normal incremental displacement at the discontinuity (solved by static condensation) does not approach zero (converged state), but simply changes sign with each iteration.

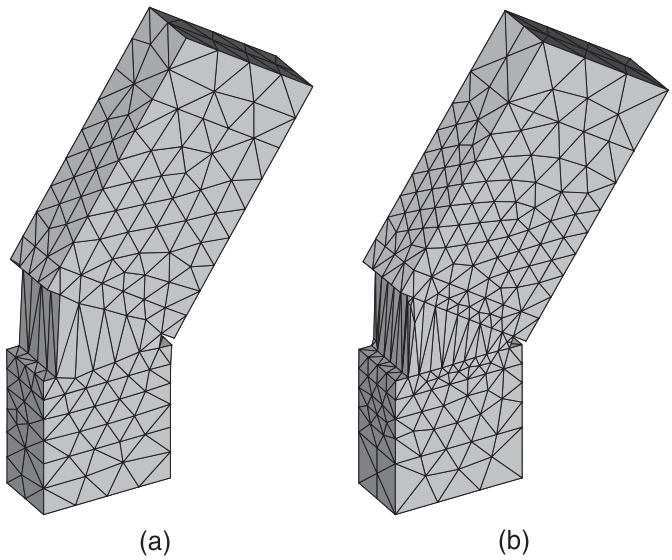

Fig. 9. Deformed specimen: (a) mesh with 1534 elements and (b) mesh with 3741 elements (non-symmetric formulation).

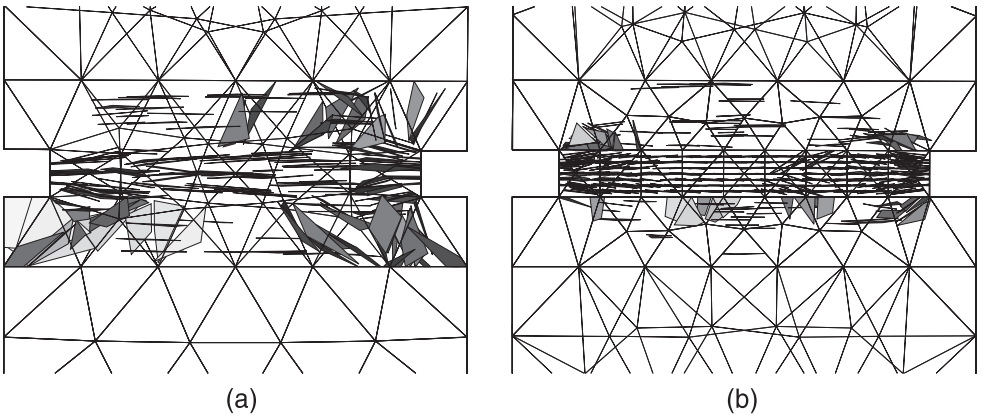

Fig. 10. Plane view of embedded crack patterns for (a) mesh with 1534 elements and (b) mesh with 3741 elements (non-symmetric formulation).

5.3. Single-edge-notched beam

To further examine the embedded model for a more complex problem, a single-edge-notched (SEN) beam (Fig. 11) is analysed to test the ability of the embedded model (non-symmetric) in situations where large shear stresses exist and cracking is known experimentally to be curved (Schlangen, 1993). Previously, smeared crack models have been able to reasonably reproduce the global load–displacement response of the SEN beam, but have failed to capture the correct (curved) failure pattern (De Borst, 1986; Rots, 1988; Feenstra, 1993). In order to model the failure mode correctly with a continuum model, Peerlings et al. (1998) resorted to a strain based modified Von Mises criterion for the internal damage variable, claiming that a purely principal strain type criterion is too sensitive to shear strains to properly model curved cracking in the case of the SEN beam. To study the behaviour of the embedded formulation, the fracture pattern at the peak load is examined. The material properties adopted for the analysis are: $E = 3.5 \times 10^4$ MPa, $f_t = 2.8$ MPa, $v = 0.15$, $G_f = 0.1$ N mm/mm^2. The crack shear stiffness is $d_{int} = 1.0 \times 10^2$ and $d_{\kappa=1.0} = 1.0 \times 10^{-6}$.

Fig. 12 shows the pattern of discontinuities (viewed from the side through the SEN beam) and the contour plot of the internal variable, averaged at the element nodes. The discontinuity planes near the notch are oriented in a direction consistent with experimental observations. However, it can also been seen that a crack does not propagate in the direction of the discontinuities, but rather the discontinuities form in

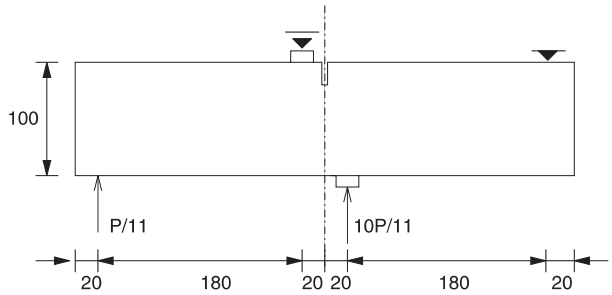

Fig. 11. Plane view of SEN beam, depth = 100 (dimensions in millimetres).

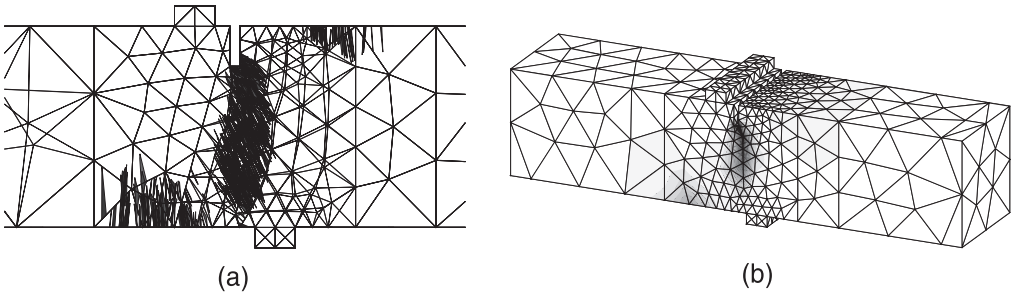

Fig. 12. SEN beam using principal stress initiation criterion: (a) crack pattern at peak load (plane view) and (b) internal variable at peak load.

layers towards the bottom of the specimen. The discontinuities are first initiated around the notch and continue directly downwards, eventually meeting the discontinuities initiated to the left of the bottom right loading plate. This result is very similar to results obtained using smeared crack models (Rots, 1988; Schlangen, 1993). In attempting to model a curved crack, propagating from the notch, here the principal stress criterion has been supplemented by the modified Von Mises criterion. The stress form of the modified criterion is given as (Williams, 1980):

$$\tfrac{1}{2}J_2 + (\sigma_c - \sigma_t)I_1 - \sigma_c\sigma_t \leqslant 0, \tag{24}$$

where I_1 is the first invariant of the stress tensor $(\mathrm{tr}(\boldsymbol{\sigma}))$ and J_2 is an invariant of the deviatoric stress tensor $(3\|\boldsymbol{\sigma}\|^2 - (\mathrm{tr}(\boldsymbol{\sigma}))^2)$. The tensile strength of the material is σ_t and the compressive strength σ_c. For the numerical example here, the compressive strength is made 10 times greater than the tensile strength. If the major tensile principal stress has exceeded the tensile strength of the material *and* the modified Von Mises yield surface Eq. (24) has been violated, a discontinuity is introduced normal to the major tensile principal stress. It can been seen in Fig. 13 that the additional condition prevents the formation of cracks moving directly downwards. The resulting crack pattern is consistent with experimental results (Schlangen, 1993).

The load–displacement responses of the models is compared with experimental results from Schlangen (1993) in Fig. 14. It can be seen that the model using the principal stress criterion predicts the peak load well, and follows reasonably the post-peak response, as smeared crack models have done in two-dimensions. The response using the modified criterion in Fig. 14 shows an overestimation of the peak load. The load–displacement response, shown here, converged numerically, and the rough response is due to the

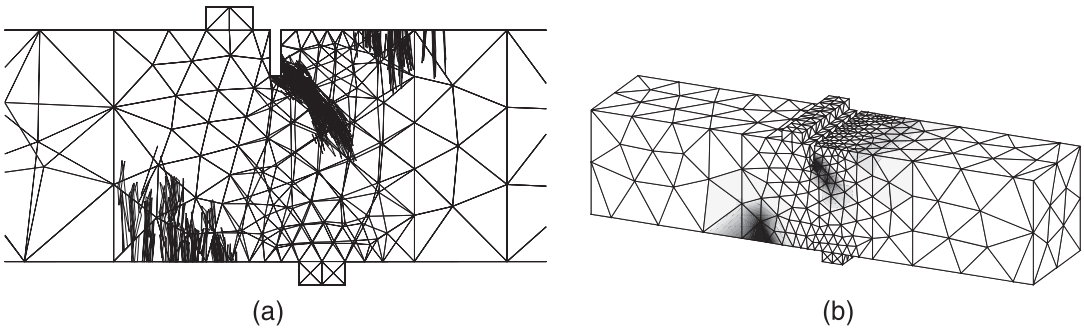

Fig. 13. SEN beam using principal stress plus modified Von Mises initiation criterion: (a) crack pattern at peak load (plane view) and (b) internal variable at peak load.

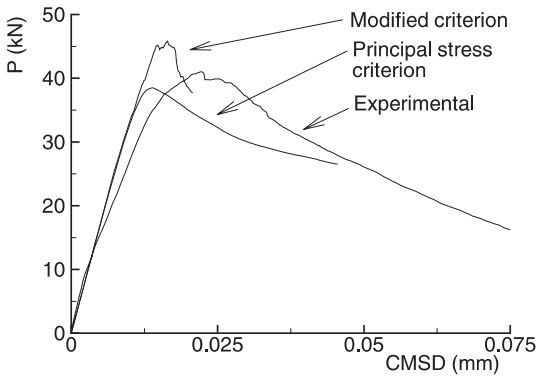

Fig. 14. Load–crack mouth sliding displacement (CMSD) response and experimental results (Schlangen, 1993) for SEN beam.

inconsistency in the initiation criterion and the constitutive model used. At initiation of a discontinuity, there can be a significant jump between the elastic maximum principal tensile stress and the normal traction across the discontinuity which leads to the rough load–displacement response and a lack of robustness past the peak load. The modified initiation criterion was introduced only to examine the effect on the pattern of cracking. For a consistently derived initiation criterion and orientation of a discontinuity, the discrete constitutive model needs to be developed from the continuum case (Oliver, 1996a).

6. Conclusions

An embedded discontinuity model has been developed as a method for performing large scale, three-dimensional calculations for the fracture of brittle materials. The numerical implementation does not require any real or artificial length scale and the constitutive model is completely independent of the finite element mesh. The ease with which traction separation relationships can be developed is very appealing for the simulation of failure in materials such as concrete, where mode-I and mode-II parameters can be addressed directly and linked to experimental data. The embedded model offers advantages over classical smeared models since no numerical parameters are required to achieve objective results and stress locking as a consequence of displacement compatibility which is avoided since the enhanced modes are incompatible. The kinematic enhancement of the non-symmetric models allows dependency on mesh alignment to be largely overcome. Conceptually, in order to accurately model fracture, the mesh need only be fine enough to capture effectively the strain field in the specimen. The example of the double notched specimen shows that the model can produce a global response that is objective with respect to the spatial discretisation.

The analyses of the double notched specimen and the SEN beam also highlights a feature unique to the three-dimensional version of the model. While the constitutive model is discrete, it can be seen that the cracking pattern is very diffuse, unlike what has been observed in two dimensional models. This effect can be largely attributed to the increased complexity of finding a path through an unstructured three-dimensional mesh. It is not always possible to easily identify a single discrete crack propagating through the specimens, but rather a diffuse band of discontinuities. As with other models in three dimensions, this can lead to a loss of robustness when a number of integration points lie close to the boundary between the damaging (localising) region and the elastically unloading region. At these points, the sign of the loading function may begin to oscillate during the iterative process. Experience here indicates that this problem becomes more severe upon mesh refinement.

From the numerical results, it is concluded that the embedded model is capable of producing a global response that is insensitive to element size and to an extent element orientation in coarse three-dimensional meshes. The use of discrete constitutive models does not make this a truly discrete approach with genuine separation, but rather a continuum model with special enhancement of the local strain field by considering the extreme case when a continuum model collapses onto a line. By doing this, no numerical parameters dependent on the spatial discretisation are required.

Acknowledgements

This research is supported by the Technology Foundation STW, applied science division of NWO and the technology programme of the Ministry of Economic Affairs, Netherlands.

References

Armero, F., Garikipati, K., 1996. An analysis of strong discontinuities in multiplicative finite strain plasticity and their relation with the numerical simulation of strain localization. International Journal of Solids and Structures 33 (20–22), 2863–2885.

Askes, H., Sluys, L.J., 2000. Remeshing strategies for adaptive ALE analysis of strain localisation, European Journal of Mechanics A/Solids, (in press).

Belytschko, T., Fish, J., Engelmann, B.E., 1988. A finite element with embedded localization zones. Computer Methods in Applied Mechanics and Engineering 70, 59–89.

De Borst, R., 1986. Nonlinear analysis of frictional materials. Ph.D. Thesis, Delft University of Technology, Netherlands.

De Borst, R., Sluys, L.J., Mülhaus H.B, H.B, Pamin, J., 1993. Fundamental issues in finite element analyses of localization and deformation. Engineering Computations 10, 99–121.

Feenstra, P.H., 1993. Computational aspects of biaxial stress in plain and reinforced concrete. Ph.D. Thesis, Delft University of Technology, Netherlands.

Larsson, R., Runesson, K., 1996. Element-embedded localization band based on regularized displacement discontinuity. ASCE Journal of Engineering Mechanics 122 (5), 402–411.

Lotfi, H., Shing, P.B., 1995. Embedded representation of fracture in concrete with mixed finite elements. International Journal for Numerical Methods in Engineering 38, 1307–1325.

Oliver, J., 1996a. Modelling strong discontinuities in solid mechanics via strain-softening constitutive equations, part 1: fundamentals. International Journal for Numerical Methods in Engineering 39, 3575–3600.

Oliver, J., 1996b. Modelling strong discontinuities in solid mechanics via strain-softening constitutive equations, part 2: numerical simulation. International Journal for Numerical Methods in Engineering 39, 3601–3623.

Oliver, J., Simo, J.C., 1994. Modelling strong discontinuities by means of strain-softening constitutive equations. In: Mang, H., Bićanić, N., De Borst, R., EURO-C 1994 Computer Modelling of Concrete Structures, Pineridge Press, Innsbruck, Austria, 363–372.

Ortiz, M., Leroy, Y., Needleman, A., 1987. A finite element method for localized failure analysis. Computer Methods in Applied Mechanics and Engineering 61, 189–214.

Peerlings, R.H.J., De Borst, R., Brekelmans, W.A.M., Geers, M.G.D., 1998. Gradient-enhanced damage modelling of concrete fracture. Mechanics of Cohesive Frictional Materials 3, 323–342.

Pijaudier-Cabot, G., Bažant, Z., 1987. Nonlocal damage theory. ASCE Journal of Engineering Mechanics 113 (10), 1512–1533.

Rots, J.G., 1988. Computational modeling of concrete fracture. Ph.D. Thesis, Delft University of Technology, Netherlands.

Schlangen, E., 1993. Experimental and numerical analysis of fracture processes in concrete. In: Heron, vol. 38 (2), Delft University of Technology and TNO Building and Construction Research, Netherlands.

Simo, J.C., Oliver, X., Armero, F., 1993. An analysis of strong discontinuities induced by strain-softening in rate-independent inelastic solids. Computational Mechanics 12, 277–296.

Simo, J.C., Rifai, M.S., 1990. A class of mixed assumed strain methods and the method of incompatible modes. International Journal for Numerical Methods in Engineering 29, 1595–1638.

Sluys, L.J., 1997. Discontinuous modelling of shear banding. In: Owen, D.R.J., Oñate, E., Hinton, E. (Eds.)., Computational Plasticity Fundamentals and Applications. CIMNE, Barcelona, Spain, pp. 735–744.

Sluys, L.J., Berends, A.H., 1998. Discontinuous failure analysis for mode-I and mode-II localization problems. International Journal of Solids and Structures 35 (31–32), 4257–4274.

Taylor, R.L., Simo, J.C., Zienkiewicz, O.C., Chan, C.H., 1986. The patch test – a condition for assessing FEM convergence. International Journal for Numerical Methods in Engineering 22, 39–62.

Van Vliet, M.R.A., Van Mier, J.G.M., 1999. Effect of strain gradients on the size effect of concrete in uniaxial tension. International Journal of Fracture 95 (1–4), 195–219.

Wells, G.N., Sluys, L.J., 2000. Application of embedded discontinuities for softening solids. Engineering Fracture Mechanics 65, 263–281.

Williams, J.G., 1980. Stress Analysis of Polymers, 2nd ed. Ellis Horwood, Chichester.